Materials and Coatings Fabricated Using the Additive Manufacturing Technologies
Материалы и покрытия, получаемые методами аддитивных технологий

UDC 621.762.2

https://doi.org/10.17073/1997-308X-2024-1-40-51

Research article
Научная статья

Synthesis of $(TiTaNb)_xHf_yZr_zC$ high-entropy carbides resistant to high thermal oxidation by mechanical alloying and spark plasma sintering

A. E. Kim, N. E. Ozerskoi, N. G. Razumov, E. V. Volokitina, A. A. Popovich

Peter the Great St. Petersburg Polytechnic University
29 Polytekhnicheskaya Str., St. Petersburg 195251, Russian Federation

nikolaiozerskoi@yandex.ru

Abstract. This study presents the synthesis of (TiZrHfTaNb)C, $(TiTaNb)_{0.45}Hf_{0.275}Zr_{0.275}C$ and $(TiTaNb)_{0.3}Hf_{0.35}Zr_{0.35}C$ single-phase, high-entropy carbides through mechanical alloying and plasma sintering. High-entropy carbides hold promise for applications in jet engine components. We identified optimal mechanical alloying conditions to achieve powder homogeneity and minimize iron fouling. The microstructure, phase, and chemical compositions of the samples were investigated. At 1600 °C, a sample with a face-centered cubic (FCC) lattice and low content of zirconium and hafnium oxides was formed. Elevating the sintering temperature to 2000 °C facilitated oxide dissolution and the formation of single-phase, high-entropy carbides. The microhardness of the samples ranged from 1600 to 2000 HV, while the compressive strength varied between 600 and 800 MPa. Plasma heating tests demonstrated excellent resistance to thermal oxidation for $(TiTaNb)_{0.3}Hf_{0.35}Zr_{0.35}C$, withstanding temperatures up to 2250 °C.

Keywords: high-entropy alloys, high-entropy carbides, mechanical alloying, sparking plasma sintering, resistance to thermal oxidation

Acknowledgements: The study received financial support from the Ministry of Science and Higher Education of the Russian Federation under Grant Agreement No. 075-03-2023-004.

For citation: Kim A.E., Ozerskoi N.E., Razumov N.G., Volokitina E.V., Popovich A.A. Synthesis of $(TiTaNb)_xHf_yZr_zC$ high-entropy carbides resistant to high thermal oxidation by mechanical alloying and spark plasma sintering. *Powder Metallurgy and Functional Coatings*. 2024;18(1):40–51. https://doi.org/10.17073/1997-308X-2024-1-40-51

Синтез высокоэнтропийных карбидов $(TiTaNb)_xHf_yZr_zC$ с высокими термоокислительными свойствами путем механического легирования и искрового плазменного спекания

А. Э. Ким, Н. Е. Озерской, Н. Г. Разумов,

Е. В. Волокитина, А. А. Попович

Санкт-Петербургский политехнический университет Петра Великого
Россия, 195251, г. Санкт-Петербург, ул. Политехническая, 29

nikolaiozerskoi@yandex.ru

Аннотация. Представлен синтез однофазных высокоэнтропийных карбидов (TiZrHfTaNb)C, $(TiTaNb)_{0,45}Hf_{0,275}Zr_{0,275}C$ и $(TiTaNb)_{0,3}Hf_{0,35}Zr_{0,35}C$ механическим легированием и искровым плазменным спеканием. Высокоэнтропийные карбиды (ВЭК) перспективны в качестве материала для деталей реактивных двигателей. Получен режим механического легирования, при котором достигаются однородность порошка и низкий технический намол. Проведен анализ микроструктуры, фазового и химического составов полученных образцов. ВЭК с ГЦК-структурой и небольшим содержанием оксидов циркония и гафния образуется при температуре 1600 °С. Повышение температуры спекания до 2000 °С способствует растворению оксидов и формированию однофазного ВЭК. Микротвердость образцов колебалась от 1600 до 2000 HV. Прочность образцов на сжатие составляла от 600 до 800 МПа. Согласно результатам газодинамических испытаний, сплав $(TiTaNb)_{0,3}Hf_{0,35}Zr_{0,35}C$ показал отличную термоокислительную стойкость до температуры 2250 °С.

Ключевые слова: высокоэнтропийные сплавы, высокоэнтропийные карбиды, механическое легирование, искровое плазменное спекание, термоокислительные свойства

Благодарности: Исследование выполнено при финансовой поддержке Министерства науки и высшего образования Российской Федерации (Соглашение о предоставлении субсидии № 075-03-2023-004).

Для цитирования: Ким А.Э., Озерской Н.Е., Разумов Н.Г., Волокитина Е.В., Попович А.А. Синтез высокоэнтропийных карбидов $(TiTaNb)_xHf_yZr_zC$ с высокими термоокислительными свойствами путем механического легирования и искрового плазменного спекания. *Известия вузов. Порошковая металлургия и функциональные покрытия*. 2024;18(1):41–51.
https://doi.org/10.17073/1997-308X-2024-1-40-51

Introduction

High Entropy Ceramics (HEC) represent a novel class of materials that has garnered significant interest from the global scientific community. These multicomponent ceramics exhibit superior hardness, wear resistance, and oxidation resistance compared to pure metal carbides [1–9].

Most research focuses on high-entropy carbides containing metals from Group 4 (Ti, Zr, Hf) and Group 5 (V, Nb, Ta) of the Periodic Table. These compounds form monocarbides with a cubic NaCl-type structure, wherein the metals share a common cationic FCC (face-centered cubic) sublattice while carbon occupies the anionic sublattice [10].

To date, numerous high-entropy carbides have been synthesized and investigated. primarily utilizing powder-based methods. The significant distinction lies in the manufacturing processes of high-entropy carbides, with most studies commencing with wet milling and mixing of precursors [4–11].

Metal oxides undergo a carbothermal reaction followed by compaction, spark plasma sintering, or hot isostatic pressing at temperatures ranging from 1600 to 2200 °C. Through this process, $(Ti_{0.2}Zr_{0.2}Nb_{0.2}Ta_{0.2}W)C$ [4] and $(Ti_{0.2}Ta_{0.2}Nb_{0.2}Hf_{0.2}W)C$ [5] were synthesized, along with the high-entropy carbide (CrNbMoWV)C [12]. These powders may contain impurities such as oxides, amorphous carbon, and graphite, indicating potential incompleteness of the carbothermal reaction or variations in carbon content.

The following materials were derived from metal monocarbides: (TiZrNbHfTa)C [13], (HfTaZrNb)C [14], and $(Ta_{0.25}Zr_{0.25}Nb_{0.25}Ti_{0.25})C$ [10]. However, the resulting ceramic materials exhibit inconsistent phase and chemical compositions and contain inclusions similar to the initial carbides in terms of chemical composition.

In certain studies, elemental metal powders and carbon serve as initial components, following a process similar to the aforementioned works. The following materials were synthesized from elemental

powders of metals and carbon: $(TiZrHfNbV)C_5$ [15], $(Hf_{0.2}Ta_{0.2}Zr_{0.2}Nb_{0.2}Ti_{0.2})C$ and $(Hf_{0.2}Ta_{0.2}Ti_{0.2}Mo_{0.2}Nb)C$ [16], $(TiVZrHfNb)C_5$, $(TiVZrHfTa)C_5$, $(TiZrNbHfTa)C_5$, $(TiZrNbVTa)C_5$, $(TiHfNbVTa)C_5$, $(ZrHfNbVTa)C_5$ [17], $(Ti_{0.2}Zr_{0.2}Ta_{0.2}Nb_{0.2}W_{0.2})C$ [11], (VNbMoTaW)C [18]. However, this process also entails certain drawbacks. Carbides of different metals are formed sequentially, resulting in regions with varying contents of the original elements.

In our papers [19; 20], we demonstrated that spark plasma sintering of CrNbMoWV powder, obtained through mechanical alloying (MA) produces a single-phase coating approximately 100 μm thick on the surface. This coating exhibits enhanced corrosion and wear resistance, surpassing conventional materials in these properties. For instance, the wear rate difference between the carbide layers of a high entropy alloy (0.001 cm^3) and WC–8Ni carbide (0.003 cm^3) amounts to 300 % [19]. Subsequent research revealed that single-phase, chemically homogeneous high-entropy ceramics can be synthesized from a mixture of high-entropy alloy and carbon MA powders, with the high-entropy carbide (CrNbMoWV)C being the first product of this process [12].

The objective of this study is to explore the production of single-phase, high-entropy ceramic materials with high chemical homogeneity using mechanically alloyed powders of TiZrHfNbTa HEA system and to evaluate their properties.

Materials and methods

We used elemental powders of metals Ti, Nb, Hf, Zr, and Ta (99.5 % purity) as initial components for synthesizing TiZrHfNbTa. Three materials were synthesized: TiZrHfTaNb, $(TiTaNb)_{0.45}Hf_{0.275}Zr_{0.275}$ and $(TiTaNb)_{0.3}Hf_{0.35}Zr_{0.35}$, with their compositions listed in the table. MFG-7 graphite powder served as the carbon source, introduced alongside the elemental metal powders.

For mechanical alloying, we employed a Pulverisette 4 planetary mill (Fritsch, Germany) under an argon atmosphere. Mechanical alloying occurred over a duration of 5 to 10 h at drive/bowl rpm ranging from 200 to 400. The 500 ml grinding bowls and 12 mm diameter grinding balls were constructed from high-strength carbon steel. Each sample weighed 50 g, and the ball-to-powder weight ratio was maintained at 1:20.

We conducted particle size distribution analysis of the powders using an Analysette 22 NanoTec plus particle sizer (Fritsch, Germany), applying the Fraunhofer diffraction method for calculation.

For sintering, we employed an HPD 25 spark plasma sintering furnace (FCT Systeme GmbH, Germany) with a diameter 20 mm graphite mold, operating at temperatures of 1600, 1800 and 2000 °C, with a pressure of 50 MPa and a holding time of 5 min at the maximum temperature.

For a layer-by-layer examination of phase composition followed plasma heating tests, a SmartLab *X*-ray diffractometer (Rigaku Corp., Japan) was utilized, employing CuK_α radiation (λ = 1.5406 Å) and the CBO-μ Cross Beam Optics system for grazing incidence *X*-ray diffraction (ω = 10°). The incidence angle range was 20 to 80°, and the acquisition rate was set at 0.2 deg/min. Morphological and microstructural analysis of the powder particles was conducted using a Mira 3 scanning electron microscope (Tescan, Czech Republic). The chemical composition of the powder particles was determined through polished samples and *X*-ray microanalysis, employing an INCA Wave 500 microanalysis system (Oxford Instruments Analytical, UK) integrated with the scanning electron microscope.

We conducted microhardness measurements using a Buehler microhardness tester (USA) with loads of 300 and 500 g applied to ground and polished samples along the section parallel to the height of the cylindrical sample. Measurements were taken in a straight line with a 330 μm increment from the top to the bottom of the sample. Compressive strength testing was performed using a Zwick/Roell Z050 universal testing machine (Germany).

For plasma heating tests, we employed a UPIM-200 electric arc plasma generator (Composite, Korolev), with plasma generated in the air. Transient heat flow was measured using a cold copper barrier (calorimeter). Initially, the heat flux density was set

Initial alloy compositions after MA

Исходные композиции сплавов после МЛ

Alloy	Sample weight, g					
	Ti	Zr	Nb	Hf	Ta	Total
TiZrHfTaNb	4.450	7.710	7.855	15.090	15.295	50
$(TiTaNb)_{0.45}Hf_{0.275}Zr_{0.275}$	2.932	10.246	5.691	20.046	11.085	50
$(TiTaNb)_{0.3}Hf_{0.35}Zr_{0.35}$	1.891	12.613	3.670	24.678	7.148	50

at 3.1 Mw/m^2, and subsequently increased incrementally. The heat flux density increased by 0.4 MW/m^2 at each step. Throughout the test, we recorded the surface temperature of the sample using a pyrometer and monitored the surface temperature distribution using a thermal imaging camera.

Results and discussion

The dissolution of alloying elements in the early stages of mechanical alloying (MA) exhibits similarities across all systems studied. At the onset of MA, intense plastic deformation flattens the initial powder particles, leading to their fusion and the formation of a composite. After 5 h of MA, the composite particles develop a characteristic layered structure consisting of different combinations of the initial components. With further prolongation of MA duration up to 7.5 h, the primary processes involve homogenization of chemical composition and interaction between the initial components aimed at reducing the system's free energy (Fig. 1).

When the MA period extends to 10 h, the iron fouling content increases. Specifically, the average iron content in the powder rises from 0.12 % after 7.5 h of MA to 0.59 % after 10 h of MA. The measured particle size distribution (in micrometers, average values) is as follows: at τ_{MA} = 5 h – d_{10} = 19.3, d_{50} = 47.5, d_{90} = 87.9; τ_{MA} = 7.5 h – d_{10} = 8.2, d_{50} = 18.6, d_{90} = 33.8; τ_{MA} = 10 h – d_{10} = 17.1, d_{50} = 33.6, d_{90} = 59.3.

Fig. 2 depicts the XRD patterns of the initial powder mixture and the powder after mechanical alloying for 5, 7.5 and 10 h. The observed peak broadening after MA arises from a reduction in the size of coherent scattering regions and increased micro stresses. After 5 h of MA, titanium is entirely dissolved in the VCCL lattice of niobium and tantalum. This dissolution can be attributed to the similar atomic radii of these elements (Ti = 1.45 Å, Nb = 1.43 Å, Ta = 1.43 Å). However, after 10 h of MA, small peaks of zirconium and hafnium are still present due to the relatively large size of their atoms. The mass fraction of the hexagonal phase ($P6_3/mmc$) is 17 %, with a cubic lattice parameter (Im-$3m$) is 3.387 Å. The deviation from the cubic lattice

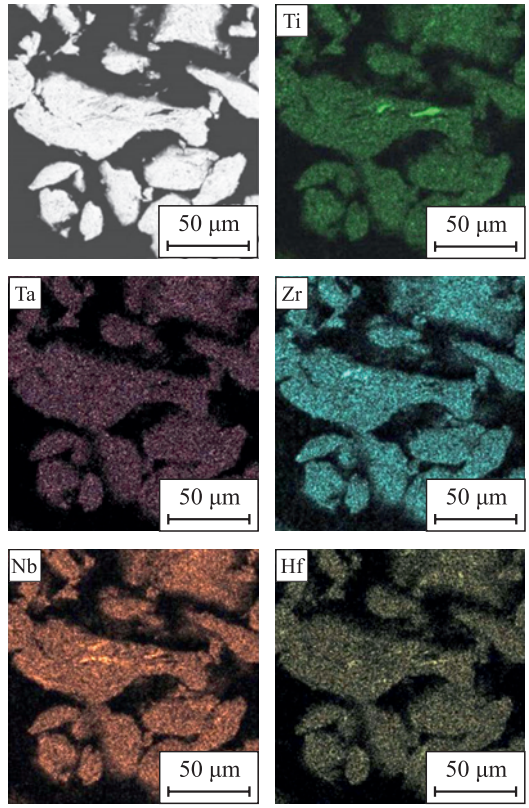

Fig. 1. Elemental distribution in TiZrHfTaNb alloy powder after τ_{MA} = 7.5 h

Рис. 1. Распределение элементов в порошке сплава TiZrHfTaNb после $\tau_{МЛ}$ = 7,5 ч

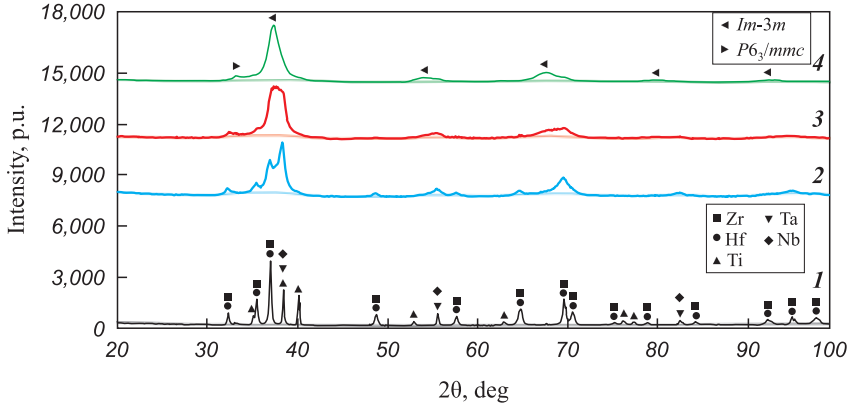

Fig. 2. Phase composition in TiZrHfTaNb powder during various MA stages

τ_{MA}, h: ***1*** – 0; ***2*** – 5; ***3*** – 7.5; ***4*** – 10

Рис. 2. Фазовый состав ВЭС-порошка TiZrHfTaNb на разных стадиях МЛ

$\tau_{МЛ}$, ч: ***1*** – 0; ***2*** – 5; ***3*** – 7,5; ***4*** – 10

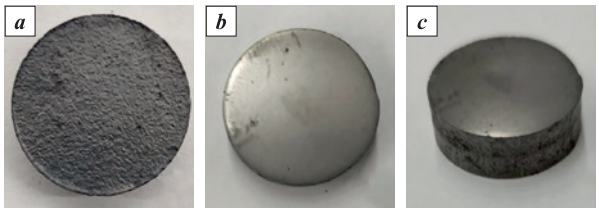

Fig. 3. Photos of (TiZrHfTaNb)C samples sintered at 2000 °C (20 mm in diameter)
a – after sandblasting; ***b–c*** – after grinding

Рис. 3. Фотографии образцов (TiZrHfTaNb)C диаметром 20 мм, спеченных при температуре 2000 °C
a – после пескоструйной обработки;
b–c – после шлифовки

parameter calculated by Vegard's law (a = 3.416 Å) for the equiatomic TiZrHfTaNb material can be attributed to the incomplete dissolution of Hf and Zr.

Based on the analysis of the microstructure, phase composition, elemental distributions, and particle size distributions of the MA samples obtained in the planetary mill, we selected τ_{MA} = 7.5 h, with a drive speed of 200 rpm and a bowl speed of 400 rpm, for the synthesis of high-entropy carbides.

High-entropy carbides were then produced from the MA powders using an FCT HPD 25 spark plasma sintering furnace. Fig. 3 displays photographs of 20 mm diameter (TiZrHfTaNb)C samples sintered at 2000 °C after undergoing sandblasting and grinding. Throughout the sintering process, we recorded various process variables including time, temperature, compression stroke, shrinkage rate, current, voltage, power, and compression force.

The experimental data obtained during the synthesis of (TiZrHfTaNb)C (Fig. 4) suggest that the process can be divided into four main stages: *1* – degassing and vacuumization; *2* – preheating; *3* – metal-carbon chemical reaction and carbide formation; *4* – compaction under 50 MPa pressure and homogenization for 5 min exposure time. These findings align with temperature profiles utilized in the solid-phase synthesis of TiC, ZrC, HfC, NbC, and TaC metal carbides [13], as well as with data obtained from spark plasma sintering of the (TiZrNbTaW)C alloy using various precursors [11].

The microstructure and phase composition of the (TiZrHfTaNb)C samples sintered at 1600 and 1800 °C reveal the presence of high-entropy HCC *Me*C carbide (*Me* = Ti, Zr, Hf, Ta, Nb), mixed zirconium-hafnium oxide, and a transition zone from the high-entropy carbide to oxide inclusions. Elevating the sintering temperature of (TiZrHfTaNb)C to 2000 °C results in increased crystal growth capacity (Fig. 5).

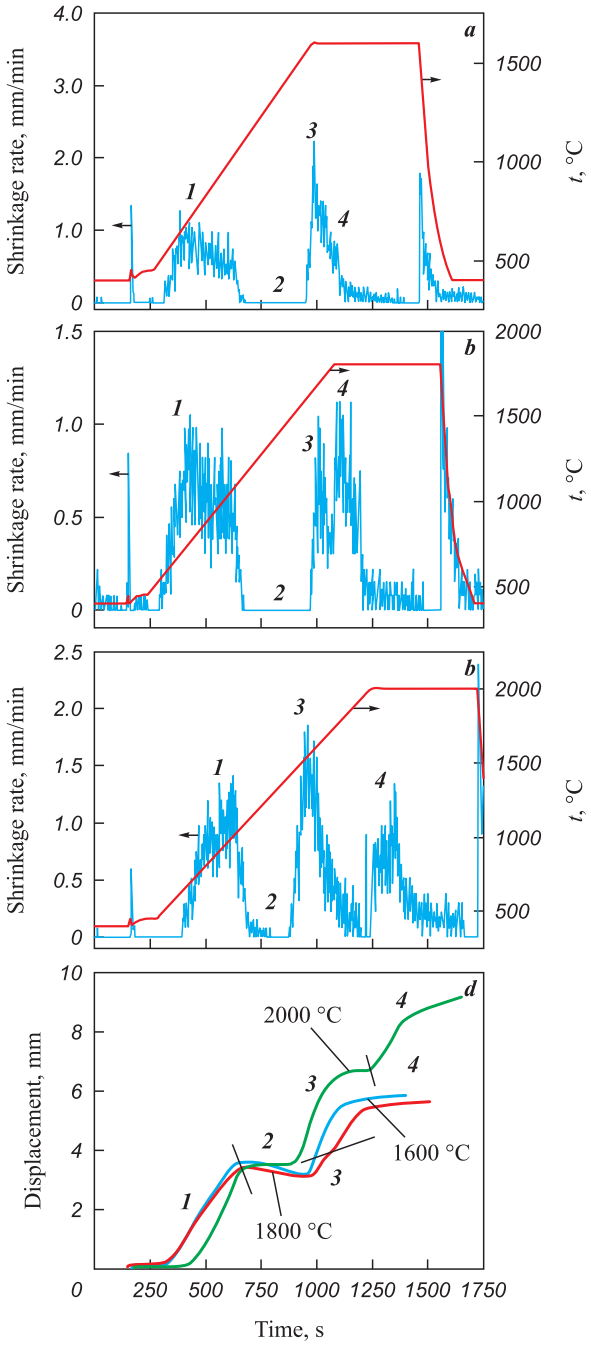

Fig. 4. Experimental curves for the synthesis of (TiZrHfTaNb)C
a–c – shrinkage rate vs. temperature and sintering time; ***d*** – compression stroke vs. time
t, °C – 1600 (***a***), 1800 (***b***), 2000 (***c***)
1–4 – synthesis stages: degassing and vacuumization (***1***), preheating (***2***), metal-carbon reaction and carbide formation (***3***), compaction under pressure (***4***)

Рис. 4. Экспериментальные кривые, полученные при синтезе ВЭК (TiZrHfTaNb)C
a–c – зависимости скорости усадки от температуры и времени спекания; ***d*** – перемещение пуансона как функция времени
t, °C – 1600 (***a***), 1800 (***b***), 2000 (***c***)
1–4 – стадии синтеза ВЭК: дегазация и вакуумирование (***1***), предварительный нагрев (***2***), химическое взаимодействие металл–углерод и образование карбида (***3***), уплотнение под воздействием давления (***4***)

The microstructure and elemental distribution of the sample sintered at t = 2000 °C (Fig. 6) indicate the formation of a homogeneous, single-phase, high-entropy carbide. The interface between zirconium-hafnium oxide and high-entropy carbide appears clear, without a zirconium-hafnium-depleted transition zone. The absence of this transition zone and the limited number of oxide inclusions, in comparison to samples sintered at lower temperatures, may suggest the completion of redox reactions and the formation of high-entropy carbides.

From the comparison of the phase composition, microstructure, and chemical homogeneity of the (TiZrHfTaNb)C samples with the thermomechanical data (Fig. 4) obtained during the synthesis, it can be inferred that the stage of chemical interaction and redox reactions (Fig. 4, stage *3*) is either completed or nearing completion when the temperature reaches 2000 °C. Stage *4* involves the densification and homogenization of the phase and chemical compositions. The formation of metal carbides is primarily driven by diffusion in the metal and carbon sublattices, with metal and carbon diffusion occurring independently [21; 22]. The diffusion rate of metals is several orders of magnitude lower than that of carbon [23]. As a result, metal diffusion significantly influences the formation of high entropy carbides and restricts the formation of secondary phases. Comparing our results with the synthesis of (TiZrNbTaW)C using a mixture of pure components and a mixture of pure carbides [11] confirms that when the starting material is a high entropy carbide, the kinetics of its formation is linear, resulting in the synthesis product being a single phase (TiZrHfTaNb)C high entropy carbide with high chemical homogeneity.

The microhardness measurements (Fig. 7) of the (TiZrHfTaNb)C samples sintered at different temperatures validate the findings from the phase composition and microstructure analysis. The samples sintered at t = 1600 and 1800 °C demonstrate high hardness levels attributed to microscopic stresses induced by the presence of non-equilibrium oxide, carbide, and transition phases. Upon increasing the sintering temperature to 2000 °C, a single-phase, high-entropy carbide is formed. The average hardness values of the samples are 1940, 1917 and 1653 HV, respectively.

We successfully synthesized $(TiTaNb)_{0.45}Hf_{0.275}Zr_{0.275}$ and $(TiTaNb)_{0.3}Hf_{0.35}Zr_{0.35}$ under the same sintering conditions as TiZrHfTaNb)C) (t = 2000 °C). These efforts resulted in obtaining single-phase $(TiTaNb)_{0,45}Hf_{0,275}Zr_{0,275}C$ and $(TiTaNb)_{0,3}Hf_{0,35}Zr_{0,35}C$ carbides.

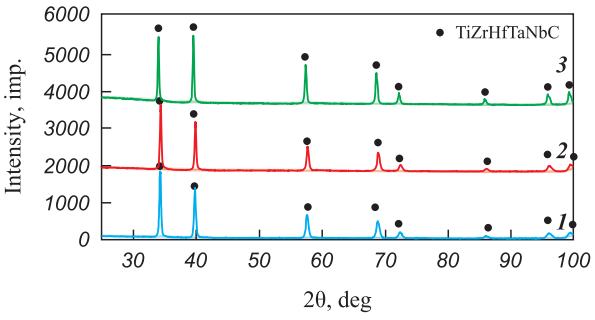

Fig. 5. Phase diagrams of (TiZrHfTaNb)C high-entropy carbides sintered at 1600 °C (*1*), 1800 °C (*2*), 2000 °C (*3*)

Рис. 5. Фазовые диаграммы высокоэнтропийных карбидов (TiZrHfTaNb)C, спеченных при температурах 1600 °C (*1*), 1800 °C (*2*), 2000 °C (*3*)

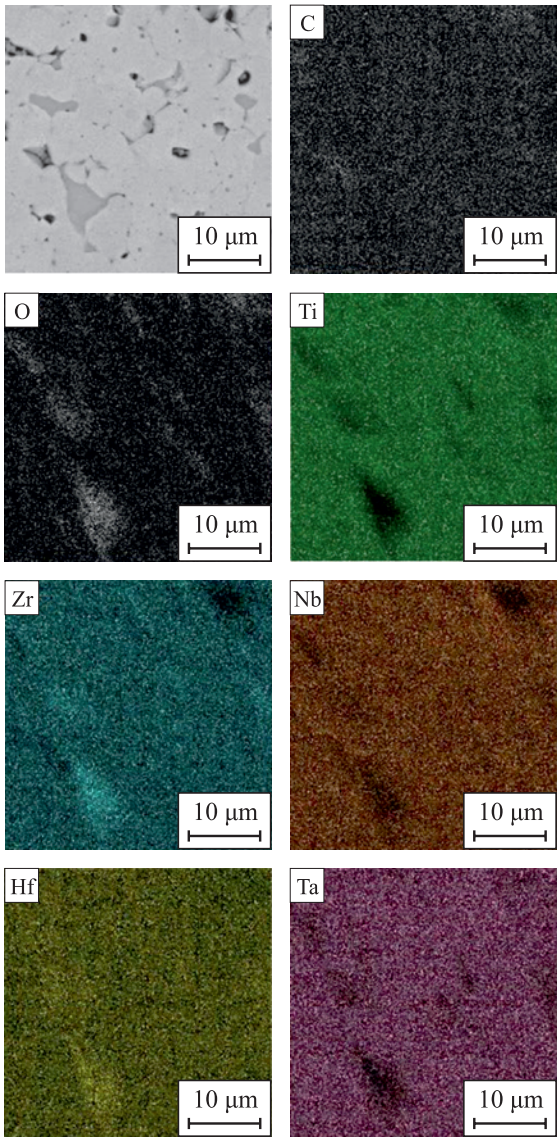

Fig. 6. Microstructure and elemental distribution of (TiZrHfTaNb)C sintered at 2000 °C

Рис. 6. Микроструктура и распределение элементов образца ВЭК (TiZrHfTaNb)C, спеченного при температуре 2000 °C

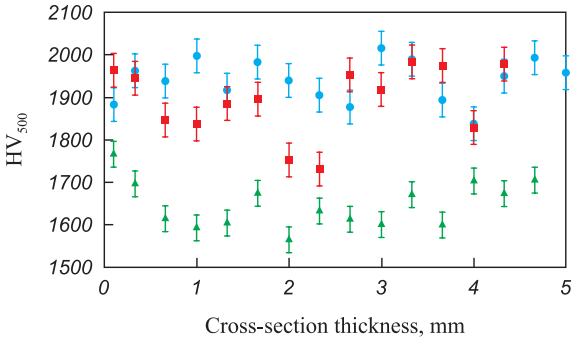

Fig. 7. Cross-sectional microhardness of the sintered (TiZrHfTaNb)C samples
t, °C: 1600 (●), 1800 (■), 2000 (▲)

Рис. 7. Микротвердость по сечению спеченных образцов (TiZrHfTaNb)C
t, °C: 1600 (●), 1800 (■), 2000 (▲)

Compression strength tests conducted on the synthesized ceramics (Fig. 8) revealed that the equiatomic (TiZrHfTaNb)C composition exhibited the highest ultimate strength of 795 MPa. As the content of Hf and Zr increased, the ultimate strength decreased to 690 for $(TiTaNb)_{0.45}Hf_{0.275}Zr_{0.275}C$ and 600 MPa for $(TiTaNb)_{0.3}Hf_{0.35}Zr_{0.35}C$, respectively.

The plasma heating tests conducted on the equiatomic (TiZrHfTaNb)C yielded unsatisfactory results (Fig. 9). Upon heating to $t = 1940$ °C, the substance melted with intense entrainment of the reaction products and base material.

The surface of the (TiZrHfTaNb)C sample following plasma heating tests exhibits regions with varying contents of the initial elements and oxygen (Fig. 10). There are three main types of elemental distribution observed: regions enriched in titanium, zirconium, and niobium; regions enriched in hafnium; and regions enriched in tantalum. The heterophase structure of the oxidation products is attributed to the differing free energies of metal oxide formation at various temperatures. During intense melting, oxidation, and entrainment of reaction products, metals with the lowest free energy of oxide formation are oxidized initially. Consequently, the resulting oxides possess different melting and evaporation temperatures, ultimately influencing the final phase composition of the reaction products.

The results of the phase composition analysis of the (TiZrHfTaNb)C sample surface after plasma heating tests (Fig. 11) validate the formation of three main phases identified through elemental distribution analysis. The hafnium-enriched phase corresponds to a mixed metal dioxide exhibiting a monoclinic lattice structure (HfO_2 prototype). The second phase, enriched in titanium, zirconium, and niobium, is characterized by the presence of mixed oxide $(TiNbZr)O_2$ with an orthorhombic lattice. This phase formation is attributed to high supercooling rates during the process, preventing the separation of the mixed oxide based on the higher niobium oxide Nb_2O_5. A similar appearance of this phase was observed during plasma heating tests of equiatomic high entropy carbide with a comparable composition. The third phase identified is the unstable TaO_2 oxide featuring a cubic lattice structure.

During testing, the $(TiTaNb)_{0.45}Hf_{0.275}Zr_{0.275}C$ and $(TiTaNb)_{0.3}Hf_{0.35}Zr_{0.35}C$ samples were subjected

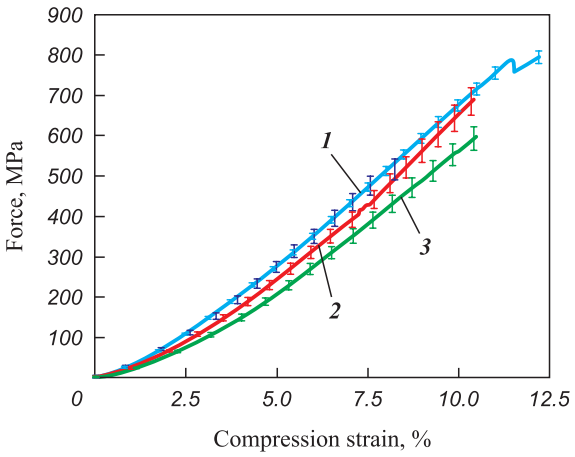

Fig. 8. Compressive strength of samples at room temperature
1 – (TiTaNbHfZr)C, ***2*** – $(TiTaNb)_{0.45}Hf_{0.275}Zr_{0.275}C$, ***3*** – $(TiTaNb)_{0.3}Hf_{0.35}Zr_{0.35}C$

Рис. 8. Прочность образцов на сжатие при комнатной температуре
1 – (TiTaNbHfZr)C, ***2*** – $(TiTaNb)_{0.45}Hf_{0.275}Zr_{0.275}C$, ***3*** – $(TiTaNb)_{0.3}Hf_{0.35}Zr_{0.35}C$

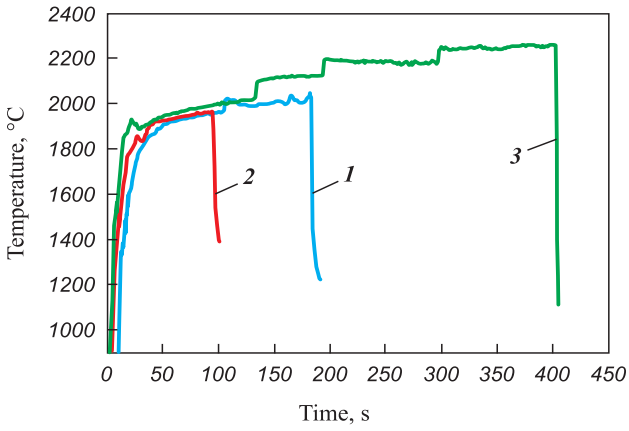

Fig. 9. Surface temperature vs. duration of plasma heating test
1 – (TiTaNbHfZr)C, ***2*** – $(TiTaNb)_{0.45}Hf_{0.275}Zr_{0.275}C$, ***3*** – $(TiTaNb)_{0.3}Hf_{0.35}Zr_{0.35}C$

Рис. 9. Зависимость температуры поверхности образцов ВЭК от длительности газодинамического испытания
1 – (TiTaNbHfZr)C, ***2*** – $(TiTaNb)_{0.45}Hf_{0.275}Zr_{0.275}C$, ***3*** – $(TiTaNb)_{0.3}Hf_{0.35}Zr_{0.35}C$

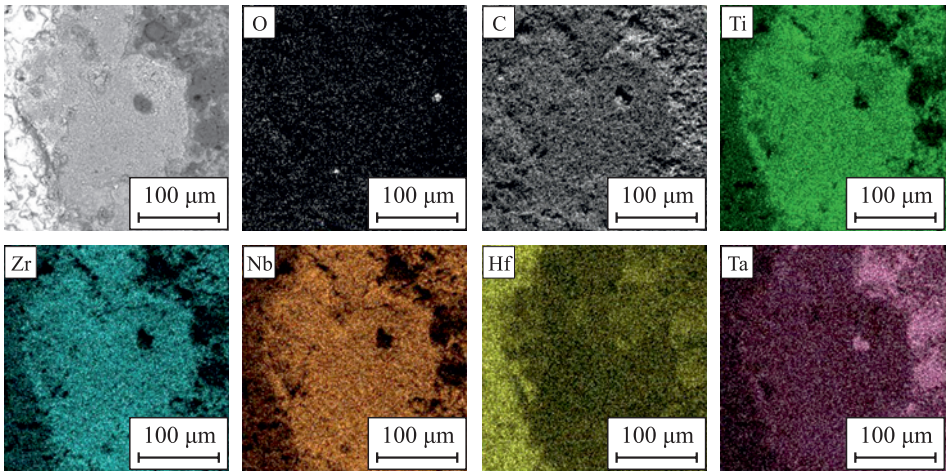

Fig. 10. Surface morphology and elemental distribution of (TiZrHfTaNb)C sample after plasma heating tests

Рис. 10. Морфология поверхности и распределение элементов образца (TiZrHfTaNb)C после газодинамических испытаний

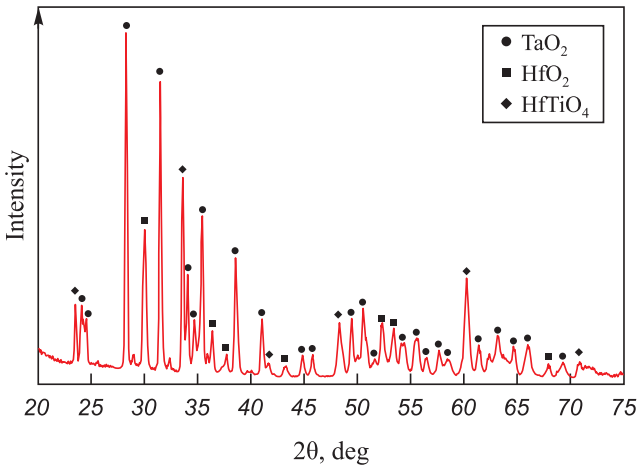

Fig. 11. XRD pattern of the oxidation products on the surface of (TiZrHfTaNb)C sample after plasma heating tests

Рис. 11. Дифрактограмма продуктов окисления на поверхности образца (TiZrHfTaNb)C после газодинамических испытаний

to an initial heat flux density of 3.1 MW/m^2, which was increased by 0.4 MW/m^2 at subsequent stages. The appearance of the samples before and after testing is illustrated in Figs. 12, *a* and 13, *a* respectively.

In the case of the $(TiTaNb)_{0.45}Hf_{0.275}Zr_{0.275}C$ sample, the transition to 3.9 MW/m^2 (τ = 170 s) resulted in burst boiling and subsequent destruction, as depicted in Fig. 12. The test was terminated after a cumulative time of 175 s, with the maximum temperature reached before sample failure being 2000 °C.

The $(TiTaNb)_{0.3}Hf_{0.35}Zr_{0.35}C$ sample underwent testing for 400 s. This demonstrated high resistance to thermal oxidation, with the surface temperature reaching 2250 °C. Subsequently, a liquid phase appeared (Fig. 13).

The layer-by-layer phase analysis of the oxidation products of the $(TiTaNb)_{0.45}Hf_{0.275}Zr_{0.275}C$ and $(TiTaNb)_{0.3}Hf_{0.35}Zr_{0.35}C$ samples revealed the segregation of layers based on the phase components (Figs. 14–16). On the surface, MeO_2 (a precursor of ZrO_2 with t_{melt} = 2715 °C); a high-melting mixed dioxide, was formed as the first layer. The second

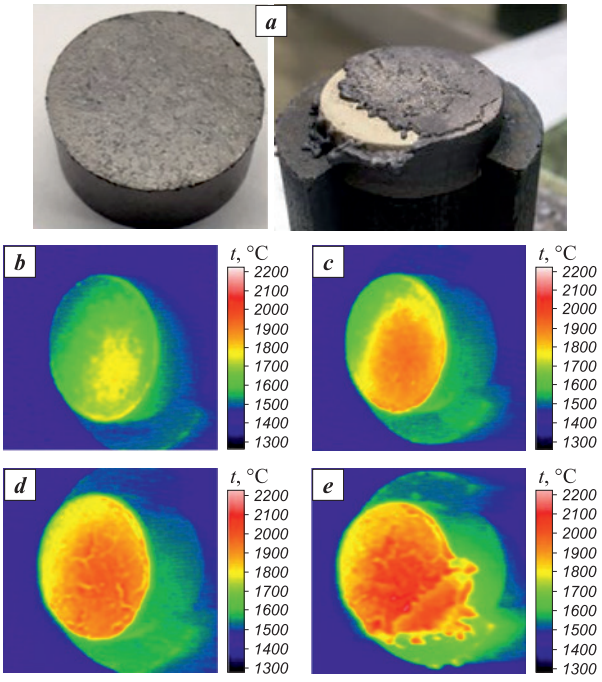

Fig. 12. $(TiTaNb)_{0.45}Hf_{0.275}Zr_{0.275}C$ sample before/after plasma heating tests (***a***) and thermal images (***b–e***)

τ, s: ***b*** – 30, ***c*** – 90, ***d*** – 150, ***e*** – 170

Рис. 12. Внешний вид образца $(TiTaNb)_{0,45}Hf_{0,275}Zr_{0,275}C$ до/после газодинамических испытаний (***a***) и термограммы испытания образца (***b–e***)

τ, с: ***b*** – 30, ***c*** – 90, ***d*** – 150, ***e*** – 170

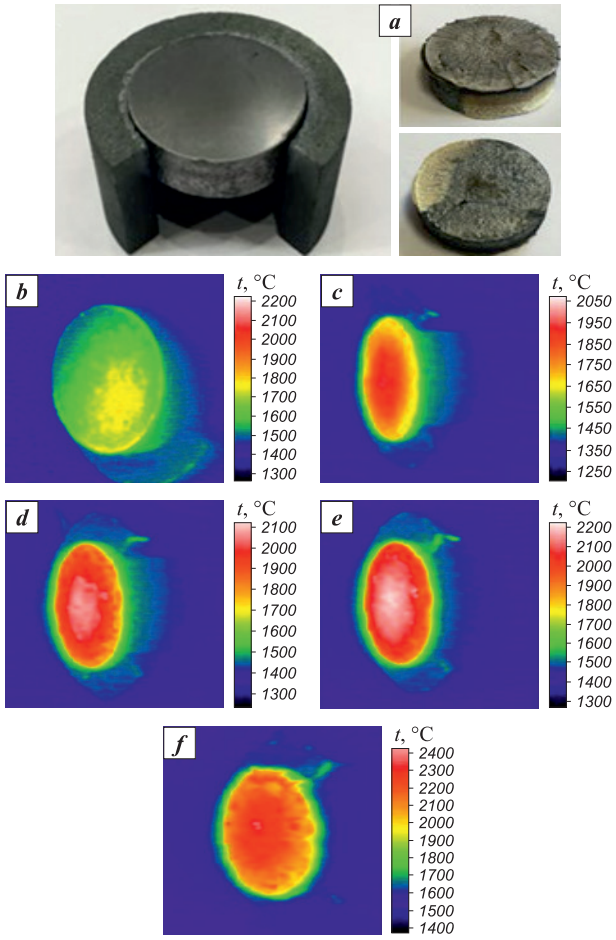

Fig. 13. $(TiTaNb)_{0.3}Hf_{0.35}Zr_{0.35}C$ sample before/after plasma heating tests (***a***) and thermal images (***b–f***)

τ, s: ***b*** – *8* (crack), ***c*** – 100, ***d*** – 150, ***e*** – 250, ***f*** – 350

Рис. 13. Внешний вид образца $(TiTaNb)_{0,3}Hf_{0,35}Zr_{0,35}C$ до/после газодинамических испытаний (***a***) и термограммы испытания образца (***b–f***)

τ, с: ***b*** – *8* (трещина), ***c*** – 100, ***d*** – 150, ***e*** – 250, ***f*** – 350

layer predominantly consists of $Me_2Me_6O_{17}$ (a precursor of $Nb_2Zr_6O_{17}$ with t_{melt} = 1670 °C); a low-melting mixed oxide. The third layer comprises Me_2O_5 (a precursor of Nb_2O_5 with t_{melt} = 1512 °C), another low-melting mixed oxide. The analysis confirms the formation of layers enriched in Zr and Hf, as well as Nb and Ta.

It is noteworthy that the $(TiTaNb)_{0.3}Hf_{0.35}Zr_{0.35}C$ sample exhibited high resistance to thermal oxidation,

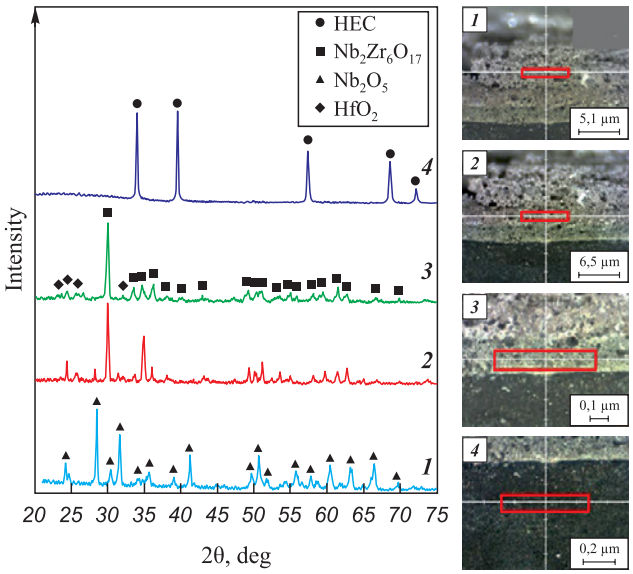

Fig. 14. Layer-by-layer phase composition analysis of $(TiTaNb)_{0.3}Hf_{0.35}Zr_{0.35}C$ sample cross-section

Areas ***1–4***: reaction products (***1***, ***2***), transition (***3***), and base material (***4***)

Рис. 14. Послойное исследование фазового состава в поперечном сечении образца $(TiTaNb)_{0,3}Hf_{0,35}Zr_{0,35}C$

1–4 – зоны: продуктов реакции (***1***, ***2***), переходной (***3***) и основного материала (***4***)

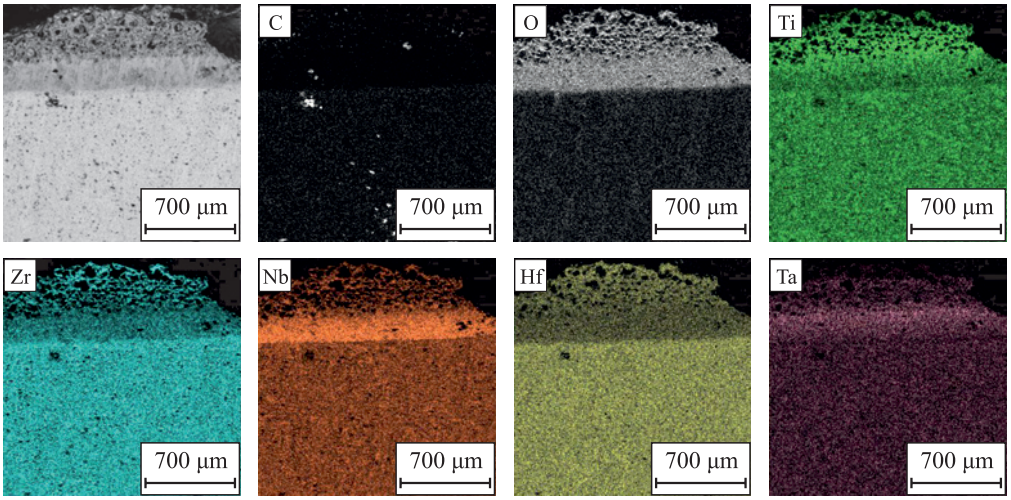

Fig. 15. Elemental distribution along the cross-section of $(TiTaNb)_{0.3}Hf_{0.35}Zr_{0.35}C$ sample

Рис. 15. Распределение элементов в поперечном сечении образца $(TiTaNb)_{0,3}Hf_{0,35}Zr_{0,35}$

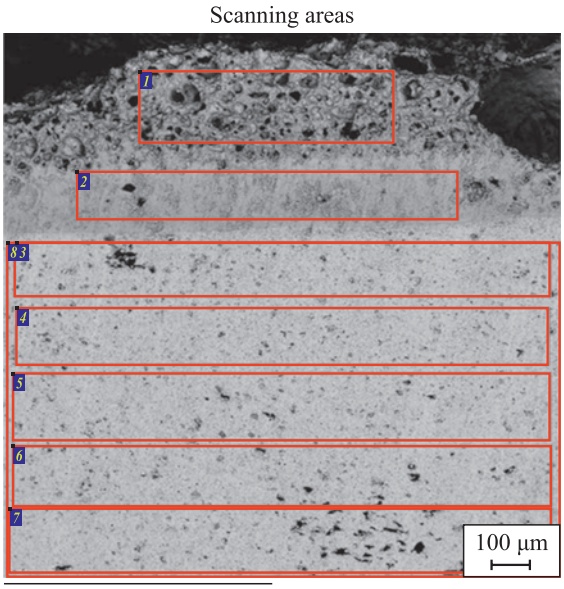

Scanning area	Elemental content, at %							
	C	O	Ti	Fe	Zr	Nb	Hf	Ta
1	22.54	56.38	3.64	0.13	5.11	1.96	7.54	2.71
2	18.79	58.23	2.41	0	4.36	6.83	4.70	4.69
3	62.69	9.56	2.71	0.23	8.38	3.11	10.61	2.70
4	58.45	9.08	3.10	0.17	10.07	3.65	12.41	3.09
5	59.83	8.44	3.14	0.53	9.66	3.50	11.88	3.03
6	62.81	8.38	2.74	0.59	8.77	3.17	10.80	2.74
7	68.22	7.37	2.34	0.41	7.26	2.66	9.38	2.36
8	62.93	8.39	2.71	0.41	8.77	3.17	10.85	2.76

Fig. 16. Elemental content in the reaction products (***1***), transition zone (***2***), and base material (***3***–***8***) in $(TiTaNb)_{0.3}Hf_{0.35}Zr_{0.35}C$ sample

Рис. 16. Содержание элементов в продуктах реакции (***1***), переходной зоне (***2***) и основном материале (***3***–***8***) образца $(TiTaNb)_{0,3}Hf_{0,35}Zr_{0,35}C$

which can be attributed to the formation of a high-melting oxide layer.

Conclusion

In summary, we have successfully synthesized single-phase, high-entropy (TiZrHfTaNb)C ceramic materials with high chemical homogeneity through mechanical alloying. This homogeneity results from the mixing of metals at the atomic level, leading to the formation of a single-phase solid solution.

Our investigation revealed that the optimal MA period is 10 h, irrespective of the initial composition. During MA, a solid solution with a face-centered cubic (FCC) lattice structure is formed, a process occurring in stages dependent on the atomic radii of the initial components. Specifically, elements with smaller atomic radii, such as Nb (0.145 nm), Ti (0.146 nm), and Ta (0.146 nm), dissolve first, followed by Hf (0.159 nm) and Zr (0.160 nm).

We have developed a process for obtaining single-phase, multicomponent ceramic materials from mechanically alloyed TiZrHfTaNb. Spark plasma sintering was utilized to investigate the physical and chemical properties of these materials. Through this process, we have successfully fabricated single-phase, equiatomic, and modified high-entropy carbides based on TiZrHfTaNb, which demonstrate resistance to high-temperature oxidation.

Furthermore, plasma heating tests revealed that resistance to thermal oxidation increases with higher Hf and Zr content. The equiatomic high-entropy carbide exhibited satisfactory results at 1900 °C. Additionally, the $(TiTaNb)_{0.3}Hf_{0.35}Zr_{0.35}C$ high-entropy ceramic material endured testing for 400 s at a surface temperature of 2250 °C.

Список литературы / References

1. Kan W.H., Zhang Y., Tang X., Lucey T., Proust G., Gan Y., Cairney J. Precipitation of (Ti, Zr, Nb, Ta, Hf)C high entropy carbides in a steel matrix. *Materialia*. 2019;1;100540. https://doi.org/10.1016/j.mtla.2019.100540
2. Braic V., Vladescu A., Balaceanu M., Luculescu C.R., Braic M. Nanostructured multi-element (TiZrNbHfTa)N and (TiZrNbHfTa)C hard coatings. *Surface Coatings Technology*. 2012;211:117–121. https://doi.org/10.1016/j.surfcoat.2011.09.033
3. Murty B.S., Yeh J.W., S. Ranganathan P.P.B. High-entropy alloys. *Advanced in Materials Science and Engineering*. 2015;1:1.
4. Zhang Y., Zhou Y.J., Lin J.P., Chen G.L., Liaw P.K. Solid-solution phase formation rules for multi-component alloys. *Advanced Engineering Materials*. 2008;10(6):534–538. https://doi.org/10.1016/j.mtla.2019.100540
5. Guo S., Ng C., Lu J., Liu C.T. Effect of valence electron concentration on stability of fcc or bcc phase in high entropy alloys. *Journal of Applied Physics*. 2011;109:103505. https://doi.org/10.1063/1.3587228
6. Zhang Y., Yang X., Liaw P.K. Alloy design and properties optimization of high-entropy alloys. *JOM*. 2012;64: 830–838. https://doi.org/10.1007/s11837-012-0366-5
7. Wang K., Chen L., Xu C., Zhang W., Liu Z., Wang Y., Zhou Y. Microstructure and mechanical properties of (TiZrNbTaMo)C high-entropy ceramic. *Journal of Materials Science and Technology*. 2020;39:99–105. https://doi.org/10.1016/j.jmst.2019.07.056
8. Yang Y., Wang W., Gan G.-Y., Shi X.-F., Tang B.-Y. Structural, mechanical and electronic properties of (TaNbHfTiZr)C high entropy carbide under pressure: Ab initio investigation. *Physica B: Condensed Matterials*. 2018;550:163–170. https://doi.org/10.1016/j.physb.2018.09.014
9. Zhang H., Hedman D., Feng P., Han G., Akhtar F. A high-entropy $B_4(HfMo_2TaTi)C$ and SiC ceramic composite. *Dalton Transactions*. 2019;48:5161–5167. https://doi.org/10.1039/c8dt04555k

10. Wang F., Yan X., Wang T., Wu Y., Shao L., Nastasi M., Cui B. Irradiation damage in $(Zr_{0.25}Ta_{0.25}Nb_{0.25}Ti_{0.25})C$ high-entropy carbide ceramics. *Acta Materialia*. 2020;195: 739–749. https://doi.org/10.1016/j.actamat.2020.06.011

11. Wei X.-F., Liu J.-X., Li F., Qin Y., Liang Y.-C., Zhang G.-J. High entropy carbide ceramics from different starting materials. *Journal of the European Ceramic Society*. 2019;39:2989–2994. https://doi.org/10.1016/j.jeurceramsoc.2019.04.006

12. Wei X.-F., Qin Y., Liu J.-X., Li F., Liang Y.-C., Zhang G.-J. Gradient microstructure development and grain growth inhibition in high-entropy carbide ceramics prepared by reactive spark plasma sintering. *Journal of the European Ceramic Society*. 2020;40:935–941. https://doi.org/10.1016/j.jeurceramsoc.2019.12.034

13. Zhou J., Zhang J., Zhang F., Niu B., Lei L., Wang W. High-entropy carbide: A novel class of multicomponent ceramics. *Ceramics International*. 2018;44:22014–22018. https://doi.org/10.1016/j.ceramint.2018.08.100

14. Csanádi T., Vojtko M., Dankházi Z., Reece M.J., Dusza J. Small scale fracture and strength of high-entropy carbide grains during microcantilever bending experiments. *Journal of the European Ceramic Society*. 2020;40:4774–4782. https://doi.org/10.1016/j.jeurceramsoc.2020.04.023

15. Chicardi E., García-Garrido C., Gotor F.J. Low temperature synthesis of an equiatomic $(TiZrHfVNb)C_5$ high entropy carbide by a mechanically-induced carbon diffusion route. *Ceramics International*. 2019;45(17):21858–21863. https://doi.org/10.1016/j.ceramint.2019.07.195

16. Moskovskikh D.O., Vorotilo S., Sedegov A.S., Kuskov K.V., Bardasova K.V., Kiryukhantsev-Korneev P.V., Mukasyan A.S. High-entropy (HfTaTiNbZr)C and (HfTaTiNbMo)C carbides fabricated through reactive high-energy ball milling and spark plasma sintering. *Ceramics International*. 2020;46:19008–19014. https://doi.org/10.1016/j.ceramint.2020.04.230

17. Chicardi E., García-Garrido C., Hernández-Saz J., Gotor F.J. Synthesis of all equiatomic five-transition metals high entropy carbides of the IVB (Ti, Zr, Hf) and VB (V, Nb, Ta) groups by a low temperature route. *Ceramics International*. 2020;46:21421–21430. https://doi.org/10.1016/j.ceramint.2020.05.240

18. Liu D., Zhang A., Jia J., Meng J., Su, B. Phase evolution and properties of (VNbTaMoW)C high entropy carbide prepared by reaction synthesis. *Journal of the European Ceramic Society*. 2020;40:2746–2751. https://doi.org/10.1016/j.jeurceramsoc.2020.03.020

19. Razumov N., Makhmutov T., Kim A., Shemyakinsky B., Shakhmatov A., Popovich V., Popovich A. Refractory crmonbwv high-entropy alloy manufactured by mechanical alloying and spark plasma sintering: Evolution of microstructure and properties. *Materials (Basel)*. 2021;14: 1–14. https://doi.org/10.3390/ma14030621

20. Makhmutov T., Razumov N., Popovich A. Synthesis of single-phase high-entropy carbides from a mixture of pre-mechanically alloyed CrNbMoWV HEA powders and carbon. *Materials Letters*. 2022;309:131363. https://doi.org/10.1016/j.matlet.2021.131363

21. Yut B.B. Nb G. of 14C in single crystals. *Crystals*. 1979;40:997–1006.

22. Zhang H., Akhtar F. Processing and characterization of refractory quaternary and quinary high-entropy carbide composite. *Entropy*. 2019;21(5):474. https://doi.org/10.3390/e21050474

23. Demaske B.J., Chernatynskiy A., Phillpot S.R. First-principles investigation of intrinsic defects and self-diffusion in ordered phases of V_2C. *Journal of Physics: Condensed Matterials*. 2017;29(24):245403. https://doi.org/10.1088/1361-648X/aa7031

Information about the Authors

Artem E. Kim – Engineer of the Laboratory "Synthesis of new materials and structures", Peter the Great St. Petersburg Polytechnic University (SPbPU)
ORCID: 0000-0002-2276-1359
E-mail: artem_7.kim@mail.ru

Nikolai E. Ozerskoi – Research Associate of the Scientific and Educational Centre "Additive Technologies", SPbPU
ORCID: 0000-0002-7371-558X
E-mail: nikolaiozerskoi@yandex.ru

Nilkolai G. Razumov – Cand. Sci. (Eng.), Head of Laboratory "Synthesis of new materials and structures", SPbPU
ORCID: 0000-0002-7147-6239
E-mail: n.razumov@onti.spbstu.ru

Ekaterina V. Volokitina – Engineer of the Russian-Chinese Research Laboratory "Functional Materials", SPbPU
ORCID: 0009-0002-5454-7733
E-mail: volokitina1606@gmail.com

Anatoly A. Popovich – Dr. Sci. (Eng.), Professor, Director of the Institute of Machinery, Materials and Transport, SPbPU
ORCID: 0000-0002-5974-6654
E-mail: popovicha@mail.ru

Сведения об авторах

Артем Эдуардович Ким – инженер лаборатории «Синтез новых материалов и конструкций» Санкт-Петербургского политехнического университета Петра Великого (СПбПУ)
ORCID: 0000-0002-2276-1359
E-mail: artem_7.kim@mail.ru

Николай Евгеньевич Озерской – научный сотрудник научно-образовательного центра «Аддитивные технологии» СПбПУ
ORCID: 0000-0002-7371-558X
E-mail: nikolaiozerskoi@yandex.ru

Николай Геннадьевич Разумов – к.т.н., заведующий лабораторией «Синтез новых материалов и конструкций» СПбПУ
ORCID: 0000-0002-7147-6239
E-mail: n.razumov@onti.spbstu.ru

Екатерина Владимировна Волокитина – инженер российско-китайской научно-исследовательской лаборатории «Функциональные материалы» СПбПУ
ORCID: 0009-0002-5454-7733
E-mail: volokitina1606@gmail.com

Анатолий Анатольевич Попович – д.т.н., проф., директор Института машиностроения, материалов и транспорта СПбПУ
ORCID: 0000-0002-5974-6654
E-mail: popovicha@mail.ru

Contribution of the Authors

A. E. Kim – planned the experiments, wrote the article, carried out the production of samples, participated in the discussion of the results.
N. E. Ozerskoi – conducted experiments, processed the obtained results, wrote the article, participated in the discussion of the results.

N. G. Razumov – critically analysed the literature, participated in the discussion of the results, formed the conclusions of the study.
E. V. Volokitina – conducted experiments, participated in the discussion of the results.
A. A. Popovich – conceptualised the idea, defined the aim of the work and its objectives, participated in the discussion of the results.

Вклад авторов

А. Э. Ким – планирование экспериментов, написание статьи, участие в обсуждении результатов.

Н. Е. Озерской – проведение экспериментов, обработка полученных результатов, написание статьи, участие в обсуждении результатов.
Н. Г. Разумов – критический анализ литературы, участие в обсуждении результатов, формирование выводов исследования.
Е. В. Волокитина – проведение экспериментов, участие в обсуждении результатов.
А. А. Попович – концептуализация идеи, определение цели работы и ее задач, участие в обсуждении результатов.

Received 28.06.2023
Revised 04.09.2023
Accepted 13.09.2023

Статья поступила 28.06.2023 г.
Доработана 04.09.2023 г.
Принята к публикации 13.09.2023 г.